

Turbulent rotating plane Couette flow: Reynolds and rotation number dependency of flow structure and momentum transport

Takuya Kawata* and P. Henrik Alfredsson†

Linné Flow Centre, KTH Mechanics, Royal Institute of Technology, SE-100 44 Stockholm, Sweden

(Received 16 February 2016; published 22 July 2016)

Plane Couette flow under spanwise, anticyclonic system rotation [rotating plane Couette flow (RPCF)] is studied experimentally using stereoscopic particle image velocimetry for different Reynolds and rotation numbers in the fully turbulent regime. Similar to the laminar regime, the turbulent flow in RPCF is characterized by roll cells, however both instantaneous snapshots of the velocity field and space correlations show that the roll cell structure varies with the rotation number. All three velocity components are measured and both the mean flow and all four nonzero Reynolds stresses are obtained across the central parts of the channel. This also allows us to determine the wall shear stress from the viscous stress and the Reynolds stress in the center of the channel, and for low rotation rates the wall shear stress increases with increasing rotation rate as expected. The results show that zero absolute vorticity is established in the central parts of the channel of turbulent RPCF for high enough rotation rates, but also that the mean velocity profile for certain parameter ranges shows an S shape giving rise to a negative velocity gradient in the center of the channel. We find that from an analysis of the Reynolds stress transport equation using the present data there is a transport of the Reynolds shear stress towards the center of the channel, which may then result in a negative mean velocity gradient there.

DOI: [10.1103/PhysRevFluids.1.034402](https://doi.org/10.1103/PhysRevFluids.1.034402)

I. INTRODUCTION

We are studying turbulent plane Couette flow (PCF) under anticyclonic, i.e., unstable, spanwise rotation (see Fig. 1 for a definition of the geometry and the coordinate system). As is usual we define the velocity along the x , y , and z directions as $U + u$, v , and w , where U is the mean velocity in the x direction and u , v , and w are the fluctuating components. The flow is characterized by two flow parameters, the Reynolds number

$$\text{Re} = \frac{U_w h}{\nu}$$

and a nondimensional rotation number, which can be expressed as

$$\Omega = \frac{2\Omega_z h^2}{\nu},$$

where $\pm U_w$ are the velocities of the walls, h is half the distance between the walls, ν is the kinematic viscosity, and the system rotation can be expressed as $\Omega = \Omega_z \mathbf{e}_z$ (\mathbf{e}_z is a unit vector along the spanwise direction). Anticyclonic rotation corresponds to $\Omega > 0$. An alternative way to describe the effect of rotation is the nondimensional rotation number written as

$$\text{Ro} = \frac{2\Omega_z h}{U_w} = \frac{\Omega}{\text{Re}}.$$

Experiments on rotating PCF (RPCF) were first reported in Refs. [1,2] and later extensively by Tsukahara *et al.* [3], who mapped the $\text{Re}-\Omega$ space in the range $0 < \text{Re} < 1000$ and $-30 < \Omega < 30$

*Corresponding author: kawata@mech.kth.se

†hal@mech.kth.se

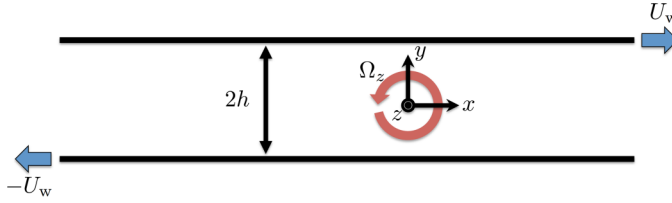


FIG. 1. Definition of rotating plane Couette flow (reproduced with permission from Ref. [4]).

with respect to different flow structures (see Fig. 2). At zero rotation the flow is transitional above about $Re = 350$ and the present study mainly focuses on Reynolds numbers in the range 500–2000 with rotation in the range $0 < \Omega < 90$ where the flow can be considered fully turbulent also at zero rotation. The stability and flow structures of RPCF in the laminar regime have also been presented in Refs. [4–6] in the form of flow visualizations and/or velocity measurements through particle image velocimetry. In Ref. [4] the same setup that is used in the present work was used, however in that case only the laminar case of $Re = 100$ was studied.

Spanwise rotating turbulent wall-bounded flows have also been studied previously through direct numerical simulations. Both rotating plane Poiseuille flow (RPPF) [7–9] and RPCF [10–13] have been simulated. The flows are different in the sense that for RPPF the mean flow vorticity changes sign in the channel, meaning that one side is stabilized (cyclonic rotation) and one side is destabilized (anticyclonic rotation), whereas for RPCF the full channel is either stabilized or destabilized.

One feature that was observed for RPPF in Ref. [7] was that in the central part of the channel a region of zero absolute vorticity, i.e., $\Omega_a = 0$, develops. Here absolute vorticity is defined as

$$\Omega_a = -\frac{dU}{dy} + 2\Omega_z.$$

This has as a consequence that the mean flow becomes asymmetric with respect to the channel centerline. Also in turbulent RPCF a similar zero absolute vorticity region develops at high enough

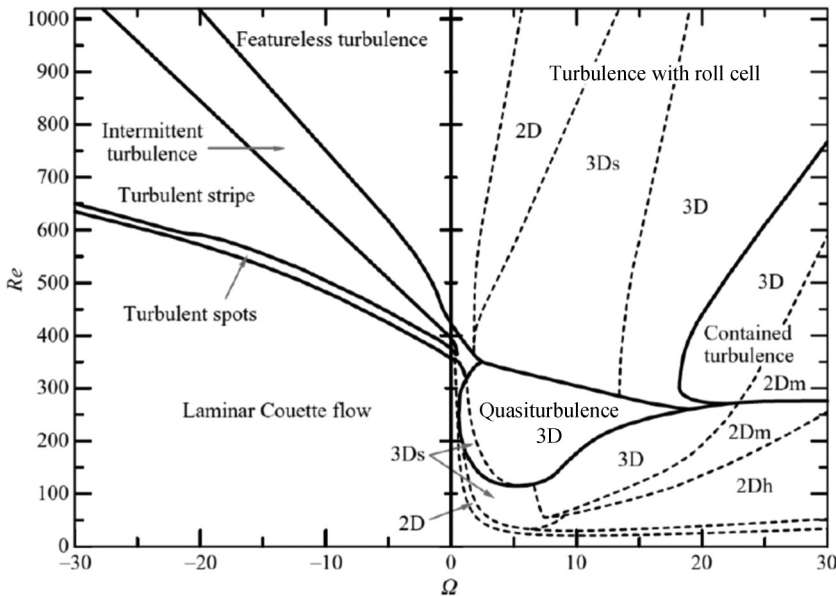


FIG. 2. The Re - Ω flow map by Tsukahara *et al.* [3]. Here $\Omega < 0$ and $\Omega > 0$ correspond to the cyclonic and anticyclonic rotation range, respectively (reproduced with permission from Ref. [3]).

rotation numbers [12]. More recently Refs. [4,6] found a similar effect also in the laminar flow region ($Re = 100$) in RPCF.

An interesting feature of both PCF and RPCF is that the total stress τ , i.e., the sum of the viscous and Reynolds stresses, is constant across the channel. This can be expressed as

$$\tau = \mu \frac{dU}{dy} - \rho \langle uv \rangle = \tau_w = \rho u_\tau^2, \quad (1)$$

where μ is the dynamic viscosity, ρ is the fluid density, $\langle \cdot \rangle$ denotes a spatial (in the xz plane) and time average, τ_w is the wall shear stress, and u_τ is the friction velocity. Hence it is possible to determine the wall shear stress (or friction velocity) from measurements of the mean velocity gradient and the Reynolds shear stress in the channel away from the walls as has been shown also for laminar, but unstable, RPCF [4].

In the present paper we study RPCF at various Reynolds numbers, $Re = 500, 1000, 1500$, and 2000 , at which the PCF is already turbulent at $\Omega = 0$. In addition to these cases $Re = 300$ was also investigated because of its interesting variation of flow structure shown in Fig. 2. For this Reynolds number the flow is laminar at $\Omega = 0$ but changes its structure into various turbulent patterns with increasing Ω . In Sec. II the flow apparatus and the stereoscopic particle image velocimetry (PIV) setup are briefly described. Section III first describes the turbulent flow field at zero rotation and thereafter the flow at various rotation rates up to $\Omega = 100$. Section IV gives a discussion of the results and shows how the flow structures change with rotation. Section V summarizes the results.

II. EXPERIMENT

A. Experimental conditions and flow apparatus

The experiments of this study were undertaken using the same flow facility as in our previous work [4], in which the PCF apparatus designed by Tillmark and Alfredsson [14,15] is mounted on a turntable together with an optical measurement system that allows stereoscopic PIV, as shown in Fig. 3(a). The PIV measurements in the rotating system are controlled from the laboratory through a local WiFi network.

The PCF apparatus is of countermoving-wall type and the working fluid is water. The outer walls of the test section consist of glass plates and the moving wall is a transparent and endless plastic film stably sliding on thin lubricating layers between the glass plates and the plastic film. This setup makes optical access to the flow field inside the channel possible. The distance between the glass walls is 20 mm and the actual distance between the countermoving walls, which corresponds to $2h$, was measured by a microscope prior to the measurement. For further details of the RPCF apparatus see Refs. [3,5].

The wall distance $2h$ and the water temperature were checked prior to the experiment and the wall speed U_w and the system rotation rate Ω_z were determined accordingly so that Re and Ω were within $\pm 1\%$ of the target value. The wall distance was $2h = 18.5$ mm in the case of $Re = 300$ and $2h = 17.6$ mm in the cases of the larger Re . As the maximum rotation rate of the turntable is 0.58 rad/s, the investigated Ω range was $0 \leq \Omega \leq 100$ for $Re = 300$ and $0 \leq \Omega \leq 90$ for $Re \geq 500$.

B. Stereoscopic PIV setup

Velocity measurements were made with a stereoscopic PIV system that allows measurements on a streamwise-spanwise plane at different y positions in a sequence. The details of the hardware setup of the PIV system were already described in Ref. [4] and are not repeated here. In short, it is a standard stereoscopic PIV system consisting of a continuous laser and two CCD cameras connected to tilt lenses. A laser beam was changed into a laser sheet parallel to the xz plane by a right-angle prism and a cylindrical lens, which are mounted on a motorized traversing stage [see Fig. 3(a)] to allow traverse of the laser sheet in the y direction. A laboratory-built water prism was used to achieve better particle image quality [see Fig. 3(b) for the camera arrangement].

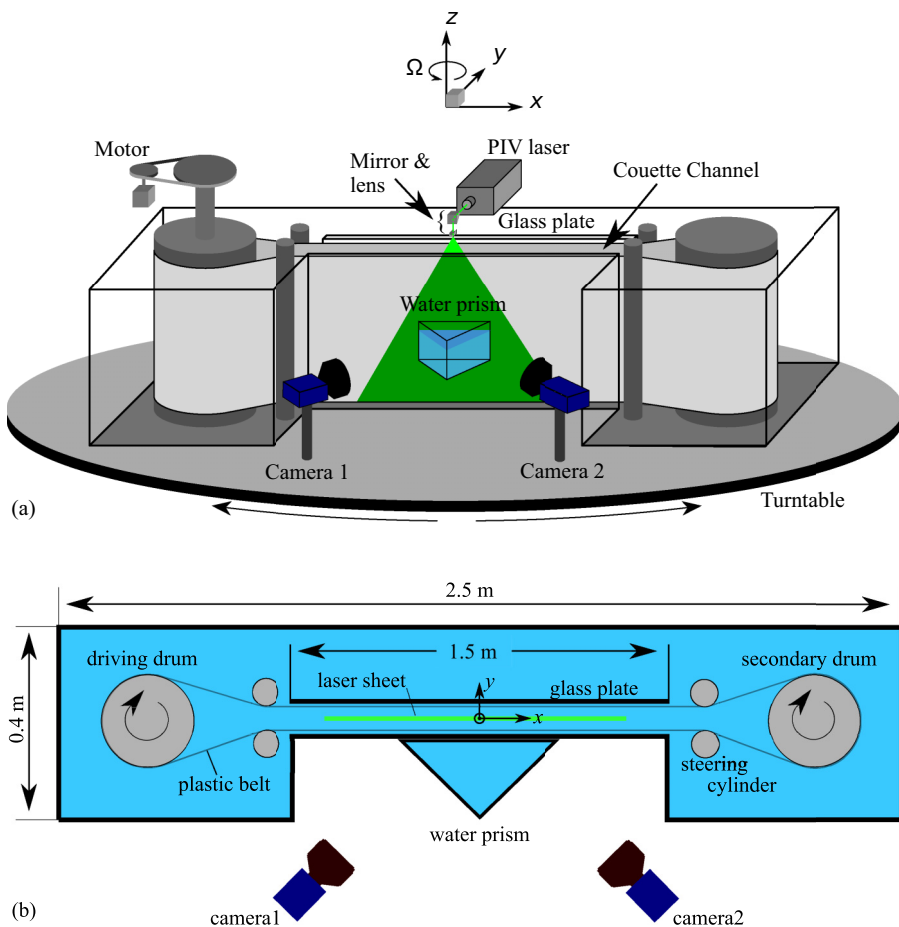


FIG. 3. Experimental apparatus of rotating plane Couette flow: (a) isometric view of the apparatus and (b) top view of the test section and camera arrangement (reproduced with permission from Ref. [4]).

The velocity measurements were carried out at several y positions in $-0.82 \leq y/h \leq 0.45$ in a sequence, starting from $y/h = -0.82$. The temporal interval between the measurements at neighboring positions was 2 s. The whole sequence took about 23 s in total. This sequence was repeated 150 times for $Re = 300$ and 500 and for $Re \geq 1000$, 200 repetitions were made.

C. Evaluation of stereoscopic PIV data

All three velocity components were evaluated from the acquired particle images by a PIV algorithm based on the fast-Fourier-transform-based cross-correlation method and the stereoscopic-reconstruction method by Soloff *et al.* [16] (see [4] for details of the algorithm and calibration procedure). The size of the interrogation area was 32×32 pixels² for the measurements of $Re = 300$ and 16×16 pixels² for those of larger Re , corresponding to 4×3.2 and 2×1.6 mm², respectively. The overlap ratio of the interrogation areas was 50%.

It was found that at high system rotation rates the evaluation of the Reynolds shear stress $-\langle uv \rangle$ was quite sensitive to the frame rate of the particle image acquisition, i.e., the resolution of the discretization, although the velocity evaluations, e.g., the values of the mean and the variance of the three components, separately were not. For the cases of $Re \geq 500$ the frame rate of the image acquisition was 117 frames/s (fps), which is the maximum frame rate of the CCD camera. To evaluate

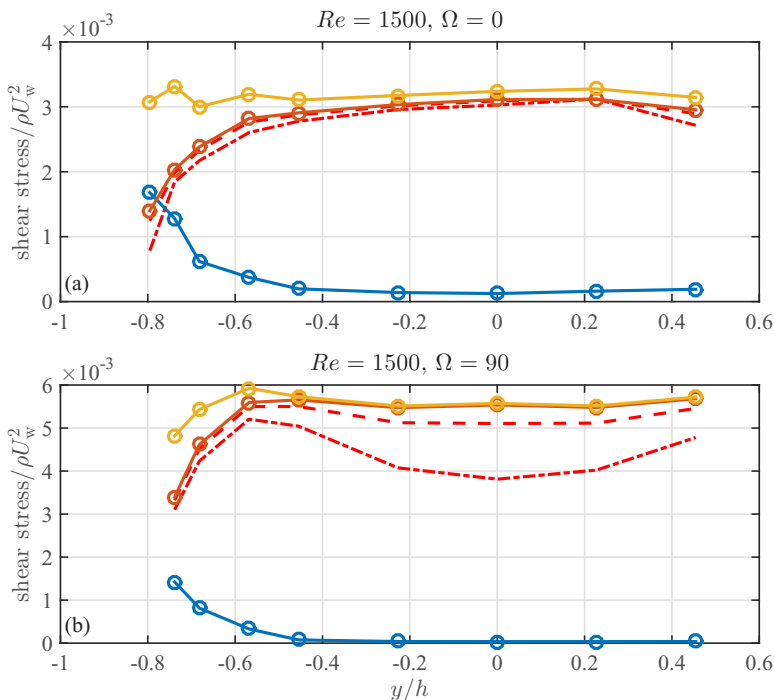


FIG. 4. Examples of the effect of the frame rate on the shear stress evaluation at (a) $Re = 1500$ and $\Omega = 0$ and (b) $Re = 1500$ and $\Omega = 90$. In each figure, the dash-dotted chained and dashed lines represent $-\langle uv \rangle$ profiles evaluated by the 2CDS with $\Delta t = 1/117$ and $2/117$ s, respectively, and the blue, red, and yellow solid lines with circles indicate the viscous, Reynolds, and total shear stress profiles obtained by the 4CDS with $\Delta t = 1/117$ s.

the velocities both a second-order central difference scheme (2CDS) and a 4CDS (using three and five image pairs, respectively) were used.

The effect of the frame rate is demonstrated in Fig. 4, showing the profiles of $-\langle uv \rangle$ measured with different frame rates and with the two discretization schemes. On the one hand, it shows that at $\Omega = 0$ the differences in the velocity evaluation do not significantly affect the results and the measured profiles of the Reynolds shear stress $-\langle uv \rangle$ and the total shear stress are fairly constant across the channel [see Eq. (1)]. On the other hand, at a high rotation rate $\Omega = 90$ the $-\langle uv \rangle$ profile obtained by the 2CDS with $2\Delta t$ ($\Delta t = 1/117$ s) is obviously not constant in the central region of the channel. However, it is clearly improved using a smaller Δt and furthermore the use of the 4CDS makes the shear even more constant. For $Re = 300$ the frame rate of the image acquisition was 15 fps and three image pairs were used for velocity evaluation, using the 2CDS.

D. Uncertainty estimates

Apart from uncertainties related to the frame rate discussed in Sec. II C, uncertainties may also arise from a limited sample size, the accuracy with which the PIV particles follow the flow, systematic errors due to the optical setup, and experimental deficiencies regarding the flow itself. We have evaluated the effect of the sample size (averaging in both space and time) and found that variations in the presented averaged quantities are negligible if the sample size is taken as half of the original and therefore conclude that the sample size is sufficient.

All of the other errors mentioned above are hard to quantify, so we estimated the limits by comparing our results with the laminar flow case in PCF at $Re = 300$, where we know that the mean

velocity profile U should be linear and that the normal and spanwise velocity components should be zero. Indeed, the V and W mean velocity components are small, less than 0.5% and 1.3% of U_w , respectively. The variances of the velocity components should all be zero in the laminar case and $\langle u^2 \rangle / U_w^2$, $\langle v^2 \rangle / U_w^2$, and $\langle w^2 \rangle / U_w^2$ are of the order of 1.6×10^{-3} , 2.9×10^{-4} , and 2.5×10^{-5} , respectively. The largest variance is for the streamwise component, which probably is due to a true variation of the streamwise velocity in the laminar case, but still quite small. If an error of the same magnitude occurred in the turbulent case it would contribute with only 6% to the variance on the centerline in the worst case.

As also shown in Fig. 4, there are some deviations from the constancy of the total shear stress close to the (left) wall. This is probably due to the increase in the mean velocity gradient close to the walls. However, from the results in the central part of the channel one may obtain an estimate of the uncertainty of the PIV results by calculating the standard deviation of the total stress obtained from the measurements. This was done for the five central measurement points and by doing so the standard deviation for various values in the range $\Omega = 0-90$ was found to be less than 2.5% for $Re = 1000$, whereas it increased for $Re = 2000$, but was still less than 4.5%.

III. RESULTS

A. Turbulent PCF without system rotation

In this section we start by showing some pertinent experimental results for the nonrotating PCF that can be used for comparison with the experiments in RPCF. Figure 5 presents representative, instantaneous velocity fields in the xz plane at the channel centerline ($y/h = 0$) comparing three Reynolds numbers, i.e., $Re = 500$, 1000, and 2000. The color shows the instantaneous streamwise velocity (i.e., the velocity in the x direction) and the arrows indicate the local velocity direction and magnitude in the xz plane. It is clear that at $Re = 500$ the color pattern indicates that there is a streaky structure that is elongated in the streamwise direction and is at least as long as the length of the measurement domain. At higher Reynolds number the smaller-scale velocity fluctuation is more apparent, but the existence of streamwise-elongated structures can still be observed (such a tendency may be more easily seen in the movie available in [17]).

By determining the two-point correlation functions in the streamwise and spanwise directions, a better quantitative measure on the structures may be obtained. For instance, the streamwise

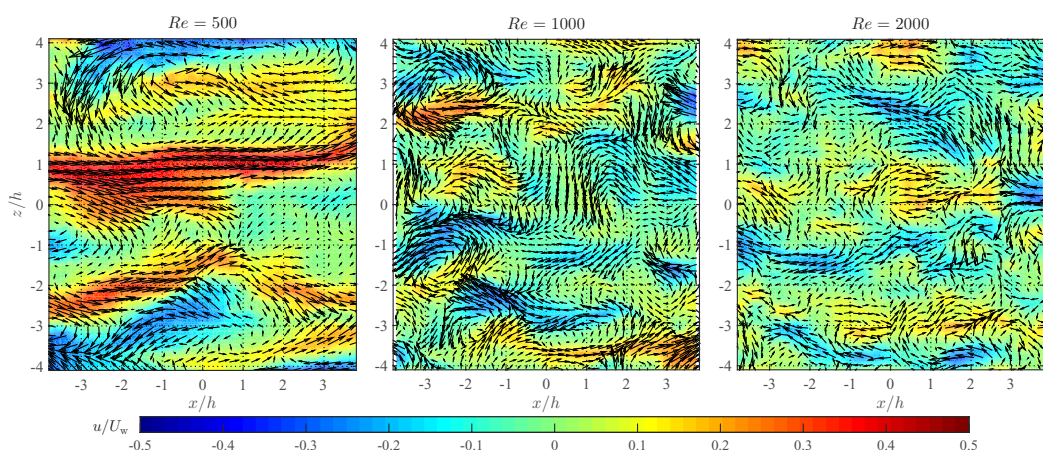


FIG. 5. Instantaneous velocity fields of turbulent PCF with no system rotation at $y/h = 0$ for $Re = 500$, 1000, and 2000. The colors indicate the streamwise velocity component and black arrows show the (u, w) vector pattern. The $2h$ length of the arrow corresponds to U_w . For readability of the figure only $1/4$ of the data points are shown for the arrows. A movie of these cases is also available in [17].

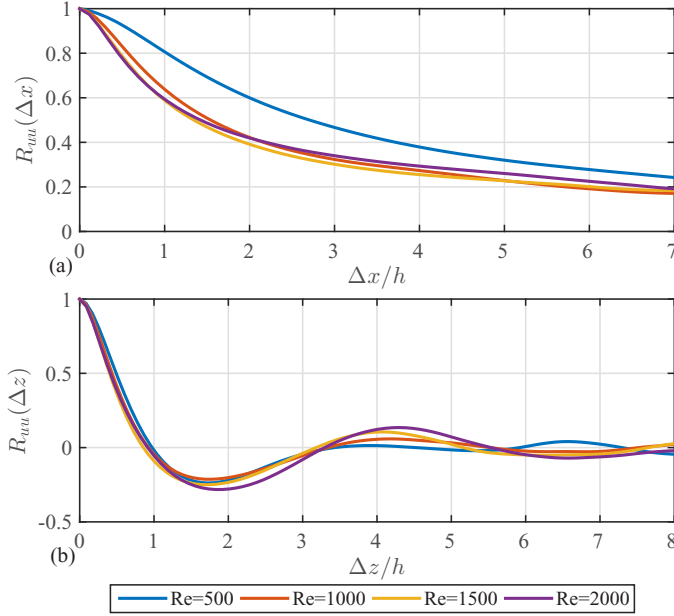


FIG. 6. Two-point space correlation function of the streamwise velocity fluctuations of turbulent PCF at $y/h = 0$ for different Reynolds numbers: (a) in the streamwise direction $R_{uu}(\Delta x)$ and (b) in the spanwise direction $R_{uu}(\Delta z)$.

correlation $R_{uu}(\Delta x)$ is obtained by a direct calculation of the correlation for different Δx and doing this for all z positions and all times. Such correlations are presented in Fig. 6. For the streamwise correlations one observes a slow decay of the correlation, reaching values around 0.2–0.25 at $\Delta x/h = 7$, where the higher value corresponds to $Re = 500$. The higher value for $Re = 500$ is a result of the strong streamwise-elongated streaky structure shown in Fig. 5. On the other hand, the spanwise correlations show a much faster decay, reaches zero around $\Delta z/h = 0.9$, and has a minimum of about -0.25 around $\Delta z/h \approx 1.8$. A second maximum is observed as well, but in this case it is the highest Reynolds number that shows the strongest correlation. These minima and maxima indicate that the flow structures have a spanwise width of approximately the channel height $2h$.

The observed behavior of the two-point correlation functions indicates the existence of coherent structures of long streamwise extent with a spanwise size close to the channel width. This can be considered to correspond to the streamwise very-large-scale structure that has been observed in the core region of turbulent PCF in many earlier studies, for example Ref. [18–20]. The Re dependency of $R_{uu}(\Delta z)$ indicates that the spanwise spacing of such a streamwise-elongated structure becomes more regular as the Reynolds number increases.

The wall shear stress was determined by averaging the total shear stress values in the central region of the channel ($-0.6 < y/h < 0.45$), obtained as the sum of the Reynolds stress and the mean flow viscous stress. From these data the friction Reynolds number $Re_\tau = u_\tau h/\nu$ was evaluated (see Fig. 4) and summarized in Table I together with the turbulence intensities and the Reynolds shear stress at the centerline of the channel. The relation between the values can be written

$$-\langle uv \rangle^+ = 1 - \frac{Re}{Re_\tau^2} \frac{d(U/U_w)}{d(y/h)}. \quad (2)$$

Note that the $-\langle uv \rangle^+$ values given in Table I are the measured values on the centerline, whereas the values of Re_τ are obtained as the average over the total shear stress values in the central region

TABLE I. The Re dependency of Re_τ and measured values of the mean velocity gradient and velocity fluctuations at the channel center.

Re	Re_τ	$dU/dy/(U_w/h)$	u_{rms}^+	v_{rms}^+	w_{rms}^+	$-\langle uv \rangle^+$
500	37	0.26	2.25	0.87	1.07	0.90
1000	63	0.20	1.89	1.02	1.22	0.95
1500	85	0.19	1.84	1.03	1.24	0.98
2000	106	0.18	1.97	1.03	1.28	1.00

of the channel. The measured values of $-\langle uv \rangle^+$ on the centerline differ slightly from those obtained from the average of the total shear stress, less than 1% for the three lower Reynolds numbers and less than 4% for the highest Re .

In Fig. 7 the friction Reynolds number is plotted as a function of Re together with results from numerical simulation studies [18–22]. The evaluated value of Re_τ increases from 37 to 106 as Re increases from 500 to 2000 and is in reasonable agreement with the numerical studies, although the experimental results at $Re = 1500$ and 2000 are somewhat smaller compared to the simulation results.

The profiles of the mean streamwise velocity are shown in Fig. 8, comparing the different Reynolds-number cases. It is shown that as the Reynolds number increases the mean velocity gradient dU/dy at the channel center decreases; these values scaled by U_w/h are also summarized in Table I. The scaled velocity gradient on the channel centerline at $Re = 500$ is 0.26 and decreases as the Reynolds number increases to 0.18 at $Re = 2000$.

The profiles of turbulence intensities and the Reynolds shear stress $\langle uv \rangle$ are also shown in Fig. 9 scaled with u_τ . The values of them at the channel center are also listed in Table I and as can be seen these values are almost constant for the different Reynolds numbers except for $Re = 500$. In Fig. 9 the profile of u_{rms}^+ at $Re = 500$ has a maximum at $y/h = -0.58$ and the peak value is 2.7. As the Reynolds number increases the maximum location moves towards the wall.

B. Turbulent RPCF

1. Flow structure

First we present some characteristic flow structures observed in the present experiment at $Re = 300$. At no rotation the flow is laminar with a linear velocity profile, but as can be seen in the Re - Ω diagram (Fig. 2), for anticyclonic rotation the flow becomes unstable and the flow structure changes

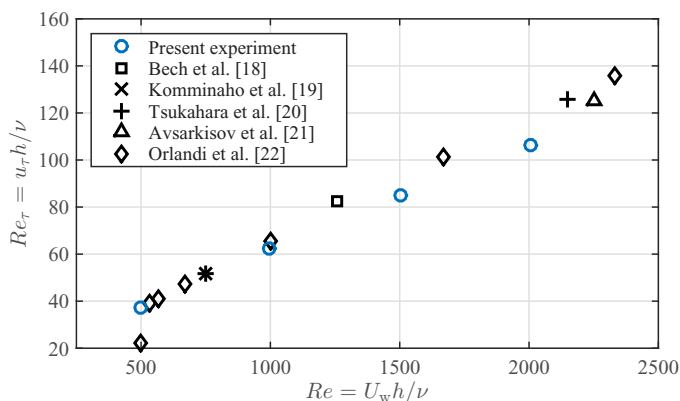


FIG. 7. Variation of Re_τ with $Re = U_w h / \nu$ for turbulent PCF. The present experimental data are compared with several earlier DNS results [18–22].

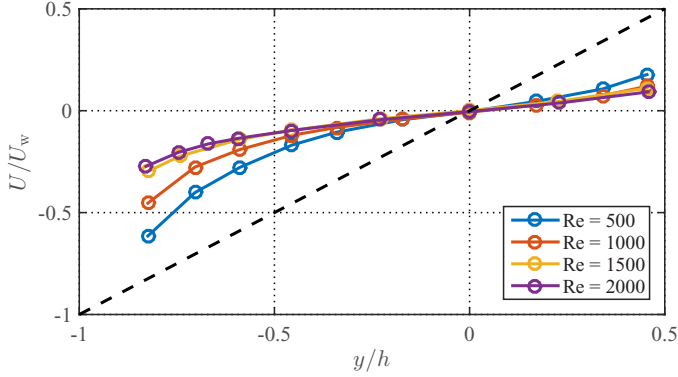


FIG. 8. Mean flow profiles of turbulent PCF at different Reynolds numbers.

as the system rotation increases. The instantaneous velocity fields at $Re = 300$ with $\Omega = 4, 20, 70,$ and 100 (corresponding to $Ro = 0.013, 0.067, 0.23,$ and $0.33,$ respectively) are presented in Fig. 10. Note that, in contrast to Fig. 5, the colors in this figure represent the wall-normal velocity component v . The $\Omega = 4$ and 20 cases fall in the *Quasiturbulence 3D* and *Contained turbulence* regimes of the $Re-\Omega$ diagram in Fig. 2, respectively, however the other rotation number cases are located outside the diagram.

At $\Omega = 4$ the roll-cell structure already shows a three-dimensional and complex flow pattern and is quite different from the straight roll cells observed at the corresponding Ω in the case of $Re = 100$ (see Ref. [4]), which in that case is the first bifurcation from the linear base flow profile. At the other rotation rate cases, however, the flow structure resembles those found at the corresponding rotation numbers at $Re = 100$: The wavy structure at $\Omega = 20$ is quite similar to the wavy roll cell that was numerically found by Nagata [23] as a tertiary flow state and experimentally observed in Refs. [3,4,6] at corresponding Ω with $Re = 100$. The straight roll cells seen at $\Omega = 70$ ($Ro = 0.23$) and the more complex roll cells with a fish-bone-like pattern at $\Omega = 100$ ($Ro = 0.33$) resemble the two-dimensional roll cells for high Ω (2Dh roll cells) defined in Ref. [3] and the twisted roll cells described in Ref. [6], which were observed at $Ro = 0.2$ and $0.4,$ respectively, at $Re = 100$.

In the case of $Re \geq 500,$ the PCF is already turbulent at zero system rotation, as described in the previous section, and with the system rotation both the coherent roll cells and smaller-scale turbulence structures coexist. Instantaneous velocity field snapshots at low and high system rotation

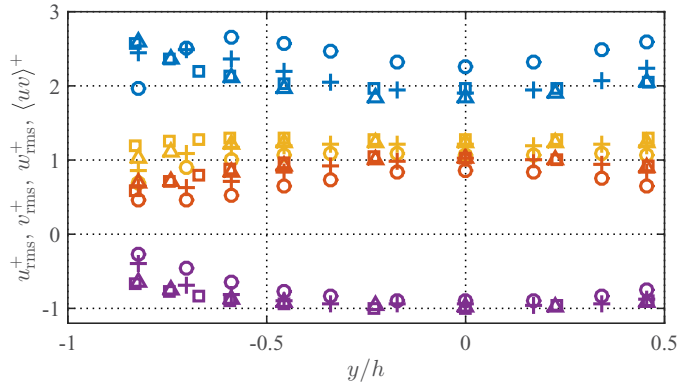


FIG. 9. Distribution of velocity fluctuations and Reynolds shear stress normalized with the friction velocity as functions of y/h for turbulent PCF: blue, u_{rms}^+ ; red, v_{rms}^+ ; yellow, w_{rms}^+ ; $\circ,$ $Re = 500;$ $+,$ $Re = 1000;$ $\Delta,$ $Re = 1500;$ and $\square,$ $Re = 2000.$

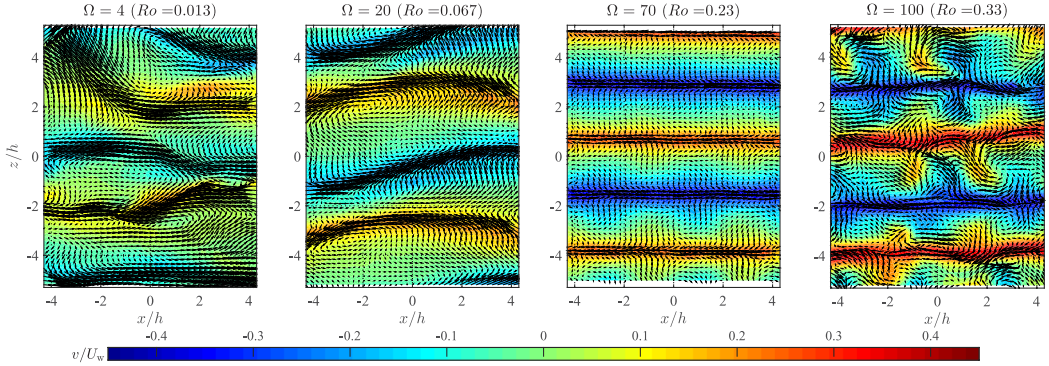


FIG. 10. Instantaneous velocity fields of the RPCF at $y/h = 0$ for $Re = 300$ with different system rotation rates. The colors and black arrows indicate the wall-normal velocity component v and the in-plane velocity vectors (u, w) , respectively. The length scale of the arrows is the same as in Fig. 5 and the arrows at all data points are shown.

rates at $Re = 500$ and 2000 are presented in Figs. 11 and 12, respectively. It is shown in Fig. 11 that at a low system rotation rate $\Omega = 4$ streamwise roll cells can be seen, but smaller-scale structures also exist, and at the higher rotation rate $\Omega = 90$ the roll cells are much clearer with a quite large variation of the wall-normal velocity component v , which indicates a strong fluid motion in the wall-normal direction by the roll-cell structure.

At higher Reynolds number the same general tendency is observed. As shown in Fig. 12, at $\Omega = 10$ the streamwise roll cells exist but cannot be so clearly seen since the small-scale turbulence fluctuations are as strong as the velocity variations due to the coherent roll cells. However, at $\Omega = 90$ the streamwise roll-cell structure can be clearly seen and it also seems that the smaller-scale fluctuation by turbulence is weakened compared to the no-rotation case. Additional movies comparing four different Ω cases at $Re = 1000$ and 2000 are also available in [17] to help the readers more easily see such a tendency of structural change at high Reynolds numbers.

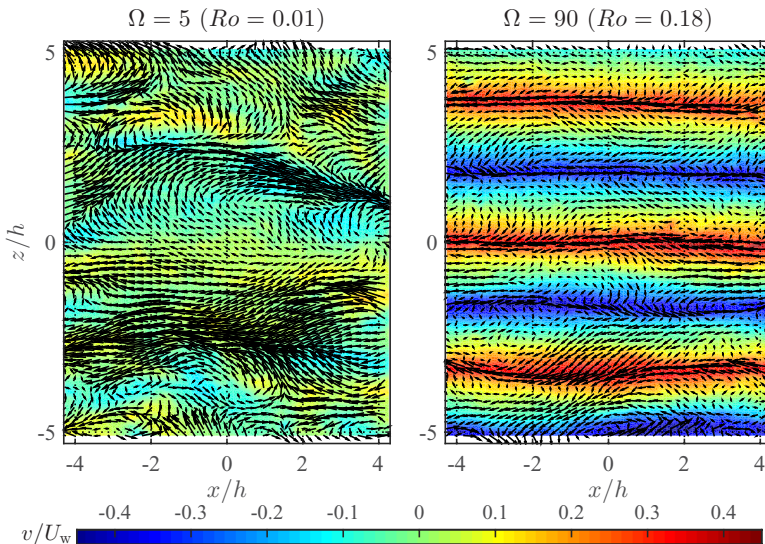


FIG. 11. Instantaneous velocity fields of turbulent RPCF at $y/h = 0$ for $Re = 500$ with low and high system rotation rate. The colors and black arrows indicate the same information as in Fig. 10 and $1/4$ of the data points are shown for the arrows.

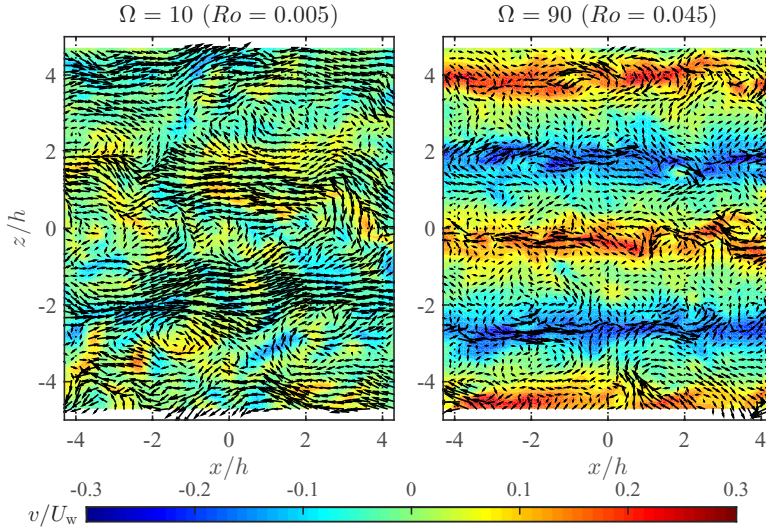


FIG. 12. Instantaneous velocity fields of turbulent RPCF at $y/h = 0$ for $Re = 2000$ with low and high system rotation rate. The colors and black arrows indicate the same information as in Fig. 10 and 1/4 of the data points are shown for the arrows.

Figures 13 and 14 show how the mean and fluctuation velocity profiles for $Re = 1000$ vary with rotation number in the range $0 \leq \Omega \leq 90$. As shown in Fig. 13, the velocity gradient at the channel center decreases as Ω increases up to $\Omega = 20$ (and actually becomes negative at $\Omega = 20$) and then the trend changes and the gradient starts to increase when the rotation increases further.

In Fig. 14 it is shown that the streamwise fluctuations u_{rms}^+ increase slightly in the channel center region with an increase from $\Omega = 0$ to $\Omega = 4$. This is probably due to an additional velocity variation induced by the roll-cell structure. However, at higher rotation rates u_{rms}^+ decreases in the channel center region with increasing rotation rate, while it increases in the region closer to the wall. On the other hand, the wall-normal component v_{rms} keeps increasing in the core region of the channel with increasing Ω , and at $\Omega = 90$ it is almost twice that of the streamwise component. This may be explained by the production terms in the energy equations for $\langle u^2 \rangle$ and $\langle v^2 \rangle$, which can be

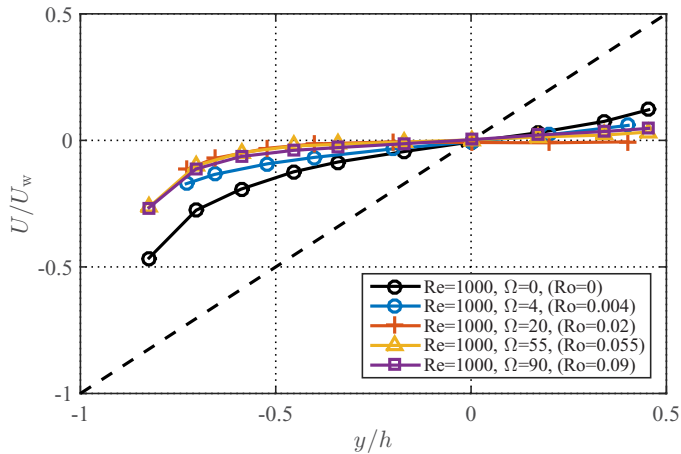


FIG. 13. Mean streamwise velocity profiles of turbulent RPCF at $Re = 1000$ and different system rotation rates.

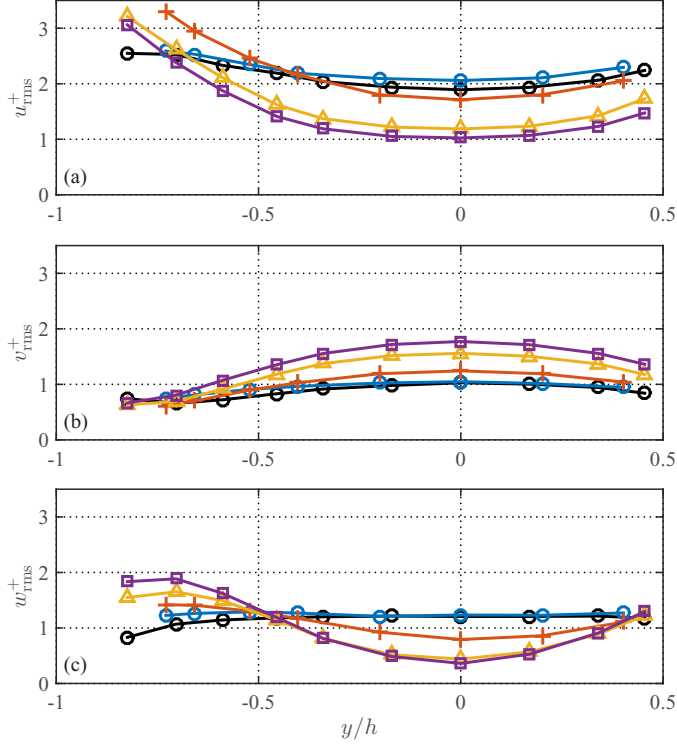


FIG. 14. Profiles of velocity fluctuations of turbulent RPCF scaled in the wall unit at $Re = 1000$ and different system rotation rates: (a) streamwise component u_{rms}^+ , (b) wall-normal component v_{rms}^+ , and (c) spanwise component w_{rms}^+ . The colors and symbols represent the same cases as in Fig. 13.

written as

$$P_{11} = -2\langle uv \rangle \frac{dU}{dy} + 4\Omega_z \langle uv \rangle, \quad (3)$$

$$P_{22} = -4\Omega_z \langle uv \rangle. \quad (4)$$

For anticyclonic rotation the rotation terms are negative and positive, respectively, for the two components (note that $-\langle uv \rangle < 0$); for details see, e.g., Ref. [4]. The spanwise component w_{rms}^+ decreases in the core region and increases in the near wall region as the system rotation increases, similarly to the streamwise component. However, there is no production of $\langle w^2 \rangle$ and these changes are probably related to the redistribution of energy from the streamwise component.

We do not show detailed results for the other measured Reynolds numbers, but the variations of both the mean flow and fluctuations distributions show generally the same tendency.

2. Wall-shear stress variation with the system rotation rate at different Reynolds numbers

The wall shear stress τ_w was evaluated based on the measured values of the total shear stress (i.e., the sum of the Reynolds shear stress and the viscous stress) in the central region of the channel. The variations with the system rotation rate at different Reynolds numbers are compared in Fig. 15. The values plotted in the figure are scaled in two different ways: In Fig. 15(a) they are scaled by the laminar value $\tau_{w,\text{lam}}$ defined as

$$\tau_{w,\text{lam}} = \mu \frac{U_w}{h}, \quad (5)$$

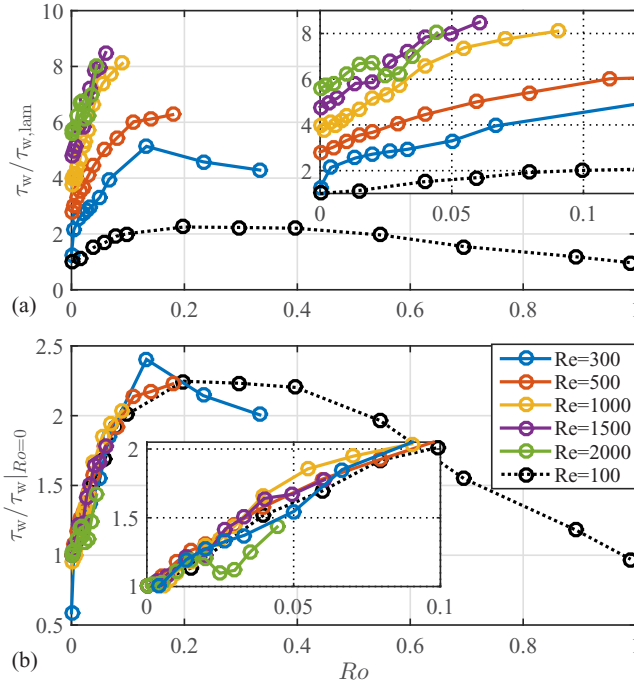


FIG. 15. Variation of wall shear stress τ_w at different Reynolds numbers as a function of Ro : (a) normalized with the laminar wall shear stress value and (b) normalized with the wall shear stress at zero rotation, except for the case of $Re = 300$, where the values are normalized by that at $Ro = 0.004$.

whereas in Fig. 15(b) they are scaled with the measured value at zero rotation, except for the case of $Re = 300$.

Since the flow at $Re = 300$ with no system rotation is laminar, the measured value of $\tau_w / \tau_{w, \text{lam}}$ should be close to one at $Ro = 0$ as in the case of $Re = 100$, while those at the larger Re start from values larger than one at $Ro = 0$. In Fig. 15(a), as the rotation number Ro increases, τ_w at $Re = 300$ increases with the system rotation rate up to $Ro = 0.2$ ($\Omega = 60$) and decreases for higher Ro . Comparing the behavior of the $Re = 300$ case in $0 \leq Ro \leq 0.067$ [corresponding to $0 \leq \Omega \leq 20$ and shown in the inset of Fig. 15(a)] to the Re - Ω diagram in Fig. 2, one can see that by increasing Ro (Ω) through this range roughly corresponds to moving from *Laminar Couette flow* through *Quasiturbulence 3D*, *Turbulence with roll cell*, and *Contained turbulence*, respectively. Therefore, the somewhat nonsmooth variation of τ_w in the low- Ro range is probably due to the transition between these different flow structures. The curves for the larger- Re cases generally increase monotonically in the investigated Ro range, except for a small local maximum observed in the cases of $Re = 1500$ and 2000 around $Ro = 0.02$ (see the zoomed-up view).

When scaling the values with the wall shear stress at zero rotation as in Fig. 15(b) the curves for all cases, except for $Re = 300$, collapse. For $Re = 300$, as mentioned above, the flow is laminar for $Ro = 0$; however, if for $Re = 300$ we instead normalize these data with the value at $Ro = 0.004$, i.e., the lowest $Ro \neq 0$, where the flow is turbulent, also these data adhere to the collapse together with the other cases. As shown in the zoomed-in view, the case of $Re = 2000$ slightly deviates from the other cases around $Ro \approx 0.02$ due to the nonsmooth variation by the small local peak.

A small local maximum in the wall shear stress observed in Fig. 15 for the high-Reynolds-number cases $Re = 1500$ and 2000 around $Ro = 0.02$ has also been observed in the numerical simulations by Salewski and Eckhardt [13], approximately at the same value of Ro . A possible explanation for this nonmonotonic behavior is that there is a change of the flow structure as Ro increases. This will

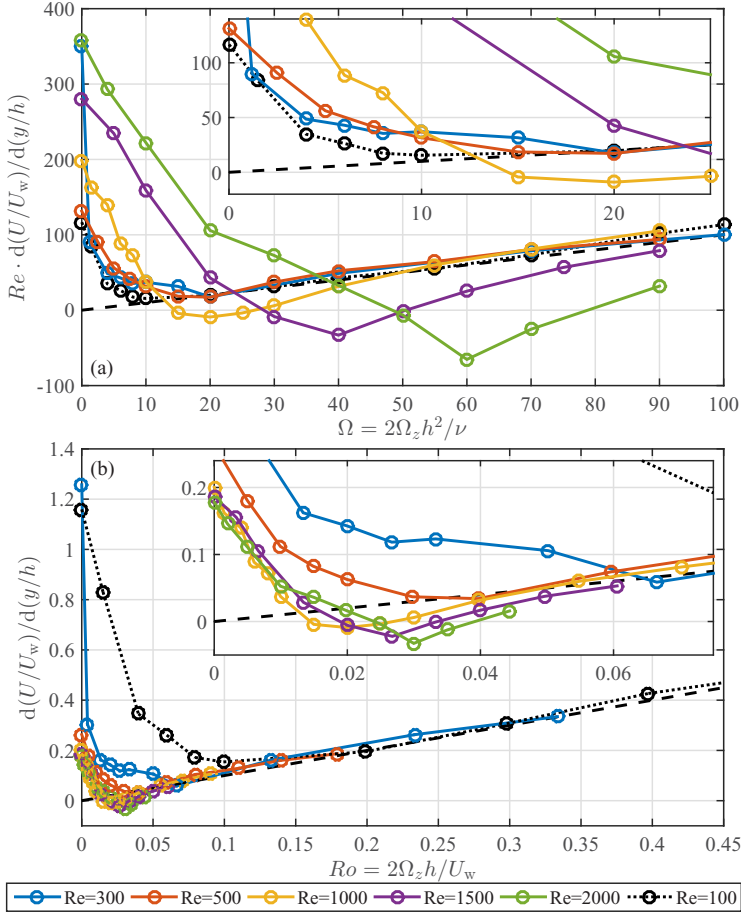


FIG. 16. Variation of mean velocity gradient $d(U/U_w)/d(y/h)$ at $y/h = 0$ with system rotation rate at different Reynolds numbers. Here Ω_z and dU/dy are scaled by (a) the viscous scale h^2/ν and (b) the shear rate h/U_w .

be further discussed in Sec. IV, where also correlation functions in the streamwise and spanwise directions are presented.

At this point one may note that although there is qualitative agreement between simulations and experiments, there are some quantitative differences when it comes to the magnitude of, for example, the wall shear stress. In Ref. [13] the Reynolds numbers within the range of our measurements are 650 and 1300 and, for instance, the wall shear stress (normalized with its laminar value) for PCF are [estimated from Fig. 2(b) therein] 3.3 and 5.3, respectively. In our case the corresponding values for 500, 1000, and 1500 are 3.7, 4.0, and 4.2, respectively.

3. Variation of mean velocity gradient at the channel centerline and the state of zero absolute vorticity

The variation of the mean velocity gradient dU/dy at the channel centerline as a function of the system rotation rate is compared for different Reynolds numbers in Fig. 16 in two different scalings. In Fig. 16(a) the system rotation rate and the velocity gradient are scaled by the viscous scale ν/h^2 , whereas they are scaled with the shear rate of the linear base flow U_w/h in Fig. 16(b). In the former

scaling the nondimensional form of the absolute vorticity $\Omega_a = -dU/dy + 2\Omega_z$ is

$$\frac{\Omega_a h^2}{\nu} = -\frac{h^2}{\nu} \frac{dU}{dy} + \frac{2\Omega_z h^2}{\nu} = -\text{Re} \frac{d(U/U_w)}{d(y/h)} + \Omega \quad (6)$$

and the state of zero absolute vorticity corresponds to $\text{Re}(d(U/U_w)/d(y/h)) = \Omega$. On the other hand, with the latter scaling the absolute vorticity is scaled as

$$\frac{\Omega_a h}{U_w} = -\frac{h}{U_w} \frac{dU}{dy} + \frac{2\Omega_z h}{U_w} = -\frac{d(U/U_w)}{d(y/h)} + \text{Ro} \quad (7)$$

and $d(U/U_w)/d(y/h) = \text{Ro}$ in the zero-absolute-vorticity state. In Figs. 16(a) and 16(b) the black dashed line represents the zero-absolute-vorticity state. Also the data from Ref. [4] for laminar flow at $\text{Re} = 100$ are shown for comparison.

In Fig. 16(a) the variation of the velocity gradient at different Re starts from different values at $\Omega = 0$ and decreases towards the line of zero absolute vorticity, i.e., $\text{Re}(d(U/U_w)/d(y/h)) = \Omega$. It can be seen that the variation at low Reynolds numbers $\text{Re} = 100, 300,$ and 500 follows a trend where it adheres to the zero-absolute-vorticity line at slightly increasing Ω as Re increases and starts following the line of the zero-absolute-vorticity state from about $\Omega = 20$ (see the zoomed-in view of the rotation number range around $\Omega = 20$, located in the inset). On the other hand, the distributions of the higher Reynolds numbers do not collapse at all.

It can also be seen that the velocity gradient at $\text{Re} = 300$ becomes larger than that for $\text{Re} = 500$ in a narrow rotation number range $8 \leq \Omega \leq 20$, where the wall shear stress profile also indicates a nonsmooth behavior. As already stated, according to the $\text{Re}-\Omega$ diagram, this rotation number range includes the border between the *Quasiturbulence 3D* and *Turbulence with roll cell*, and these somewhat nonsmooth variations of the wall shear stress and velocity gradient are probably due to such a change in the flow structure.

The dU/dy distribution shows an interesting behavior for high Reynolds numbers $\text{Re} \geq 1000$ where it overshoots the zero-absolute-vorticity state and has a negative minimum. As the Reynolds number increases, the magnitude of this negative minimum increases and the minimum location also shifts towards the higher rotation number range. As the rotation number increases, the velocity gradient approaches the line corresponding to the zero-absolute-vorticity state.

In the scaling by the shear rate of the linear base profile U_w/h shown in Fig. 16(b), the measured velocity gradients at $\text{Re} = 100$ and 300 start from about 1 at $\text{Ro} = 0$; however, in the turbulent regime at higher Reynolds numbers the velocity gradient is smaller, as expected. With this scaling the data for high Reynolds numbers $\text{Re} = 1000, 1500,$ and 2000 collapse better, while those at lower Reynolds numbers, on the other hand, do not. The collapse at high Reynolds numbers is, however, not perfect. The location of the negative minimum still shifts towards the higher rotation number range; at $\text{Re} = 1000, 1500,$ and 2000 it is at $\text{Ro} = 0.020, 0.027,$ and 0.030 , respectively. The minimum value also becomes slightly more negative as the Reynolds number increases (see the zoomed-in view). It can also be seen that at low Reynolds numbers $\text{Re} = 100, 300,$ and 500 the rotation number at which the dU/dy profile starts following the zero-absolute-vorticity line shifts towards the lower- Ro region with increasing Reynolds number, but for the higher-Reynolds-number cases the starting point of the zero-absolute-vorticity state seems to be rather independent of the Reynolds number.

IV. DISCUSSION

In this section we discuss two features observed in the experiments, namely, the narrow secondary peak of the wall shear stress at $\text{Ro} = 0.02$ and the observation that the mean velocity gradient on the centerline overshoots the state of zero absolute vorticity and has a negative minimum at about $\text{Ro} = 0.02-0.03$. In particular at $\text{Re} = 1500$ and 2000 both the narrow τ_w peak and the negative velocity gradient at the channel center are observed. We will discuss these observation based on (A)

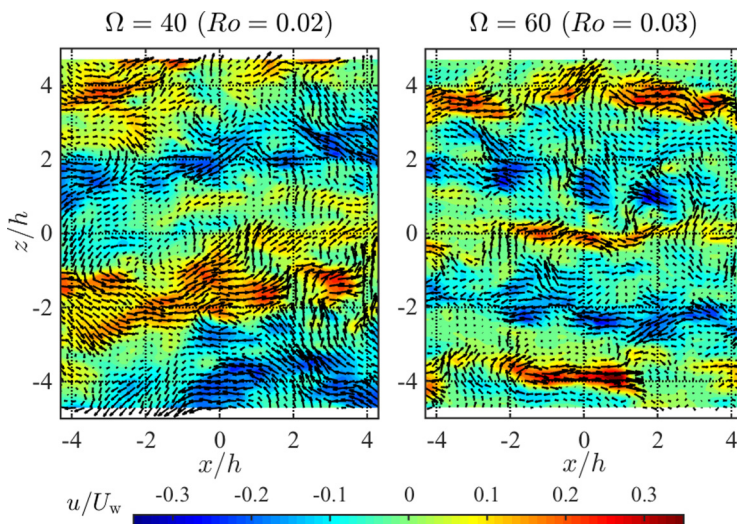


FIG. 17. Instantaneous velocity field at $y/h = 0$ for $Re = 2000$ for the case of the narrow peak of the wall shear stress ($\Omega = 40$ and $Ro = 0.02$) and for that of the negative minimum of the mean velocity gradient ($\Omega = 60$ and $Ro = 0.03$). The color and the black arrows indicate the streamwise velocity component u and in-plane velocity vectors (u, w) , respectively, and the $2h$ length of the arrow corresponds to U_w . For readability of the figures only $1/4$ of the data points are shown for the arrows.

correlation functions in the streamwise and spanwise directions and (B) production and diffusion of the Reynolds shear stress.

A. Structural information from correlation measurements

Snapshots of the instantaneous velocity field at $Re = 2000$ for $Ro = 0.02$ and 0.03 are compared in Fig. 17. It can be seen that in both cases there exist streamwise roll cells but the smaller-scale turbulence motion is also still active. Salewski and Eckhardt [13] reported that the streamwise waviness of the roll cells is the feature of roll-cell structure typically found in the flow regime of the narrow τ_w peak; also in Fig. 17 the wavy pattern of the roll cell can be seen. Furthermore, comparing the width of the roll cells in these cases, one can see that the roll cells at $Ro = 0.02$ are slightly wider than at $Ro = 0.03$.

Figure 18 presents the variation of the two-point correlation functions on the channel centerline with the system rotation rate for $Re = 500, 1000, 1500,$ and 2000 . The spanwise and streamwise two-point correlation functions are shown in the left and right columns, respectively. The spanwise correlation function $R_{uu}(\Delta z)$ shows a clear periodicity, but as the rotation number increases the periodicity is weakened, except for $Re = 500$, which shows a strong correlation also at higher Ro . At all the Reynolds numbers investigated the peak magnitude of the correlation becomes largest around $Ro = 0.01$. At this Ro the spanwise wavelength increases slightly with the Reynolds number, from $5h$ at $Re = 500$ to $6.4h$ at $Re = 2000$. For $Re = 1500$ at $Ro = 0.013$ the value of the negative correlation minimum is -0.53 , whereas the next positive peak has a value of 0.54 . This is further illustrated in Fig. 19, where also the drastic changes in the streamwise and spanwise correlations with Ro can be clearly seen, indicating that the flow structure changes in the region around $Ro = 0.02$.

The streamwise correlation function $R_{uu}(\Delta x)$ also shows a strong correlation around $Ro = 0.01$. The two streamwise and spanwise correlations indicate that the roll-cell structure at this rotation number is quite straight and regularly spaced in the spanwise direction. It is interesting to note that in the laminar case $Re = 100$ the roll-cell structure observed at the corresponding system rotation rate, i.e., $\Omega \approx 1$, takes the form of streamwise straight roll cells, which is the first bifurcation from the linear base flow.

TURBULENT ROTATING PLANE COUETTE FLOW: . . .

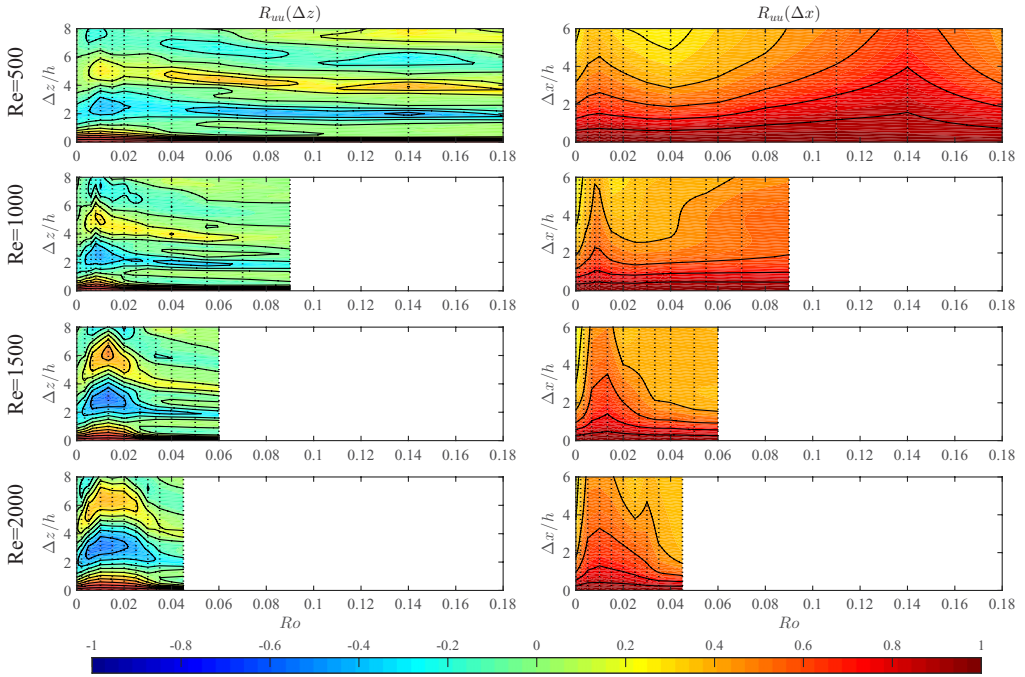


FIG. 18. Variation of the two-point correlation function at $y/h = 0$ with the system rotation rate at different Reynolds numbers: The left column shows the spanwise two-point correlation function $R_{uu}(\Delta z)$ and the right column the streamwise two-point correlation function $R_{uu}(\Delta x)$. From the top to the bottom in each column, $Re = 500, 1000, 1500,$ and 2000 . The vertical dotted lines indicate the Ro values at which the measurements are done.

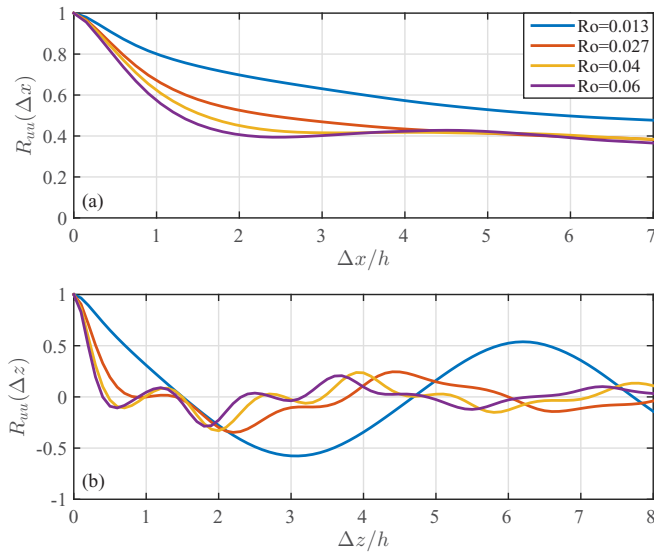


FIG. 19. (a) Streamwise and (b) spanwise correlations of the streamwise velocity at $y/h = 0$ for $Re = 1500$ in the range of $0.013 \leq Ro \leq 0.06$.

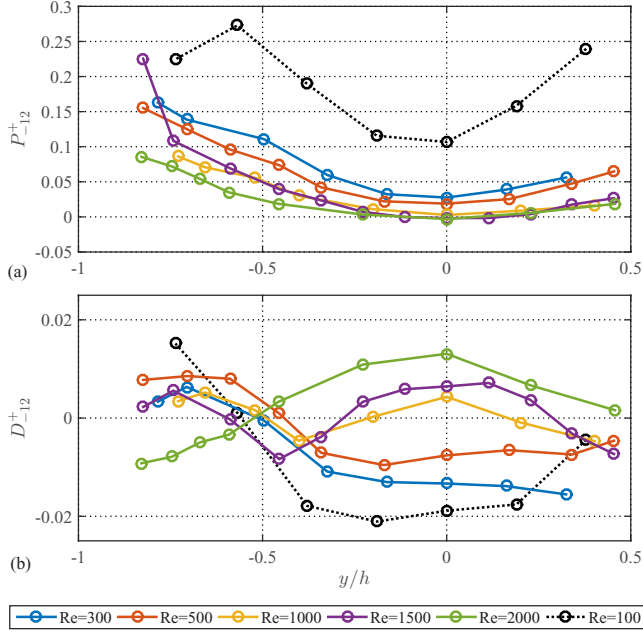


FIG. 20. Profiles of the production and the turbulent diffusion terms in the transport equation of $-\langle uv \rangle^+$ at selected rotation number for different Reynolds numbers: (a) the production terms and (b) the turbulent diffusion terms. Ω for each Re case is $\Omega = 20$ for $Re = 300, 500, \text{ and } 1000$, $\Omega = 40$ for $Re = 1500$, and $\Omega = 60$ for $Re = 2000$.

B. Production and turbulent transport of $-\langle uv \rangle$

The cause of the narrow τ_w peak and the negative velocity gradient at the channel center observed for $Ro \approx 0.02-0.03$ at $Re \geq 1000$ is further addressed in the following. The increase of τ_w and the negative dU/dy indicate that the Reynolds shear stress is significantly increased, because τ_w and dU/dy are closely related to $\langle uv \rangle$, as shown by Eq. (1). In particular, the anomalous negative velocity gradient at the channel center means that the Reynolds shear stress exceeds τ_w there. Therefore, one may expect that there would be a certain mechanism that maintains the $\langle uv \rangle$ level high at the channel center, such as the production (transport) of $\langle uv \rangle$ at (towards) the channel center. Hence one may obtain some insight into this mechanism by investigating the production and turbulent diffusion terms of the transport equation of $\langle uv \rangle$. In the RPCF the production and the turbulent transport terms of $-\langle uv \rangle^+$ can be written as

$$P_{-12}^+ = \langle u^2 \rangle^+ Ro_\tau + \langle v^2 \rangle^+ \left(\frac{dU^+}{dy^+} - Ro_\tau \right), \quad (8)$$

$$D_{-12}^+ = \frac{d\langle uv^2 \rangle^+}{dy^+}, \quad (9)$$

respectively, where Ro_τ is the system rotation rate scaled by wall units defined as

$$Ro_\tau = \frac{2\Omega_z \nu}{u_\tau^2} \left(= \frac{Re}{Re_\tau^2} Ro \right). \quad (10)$$

The distributions of P_{-12}^+ and D_{-12}^+ at the different Reynolds numbers are shown in Figs. 20(a) and 20(b) for the rotation numbers where dU/dy on the channel centerline takes the minimum at each Reynolds number.

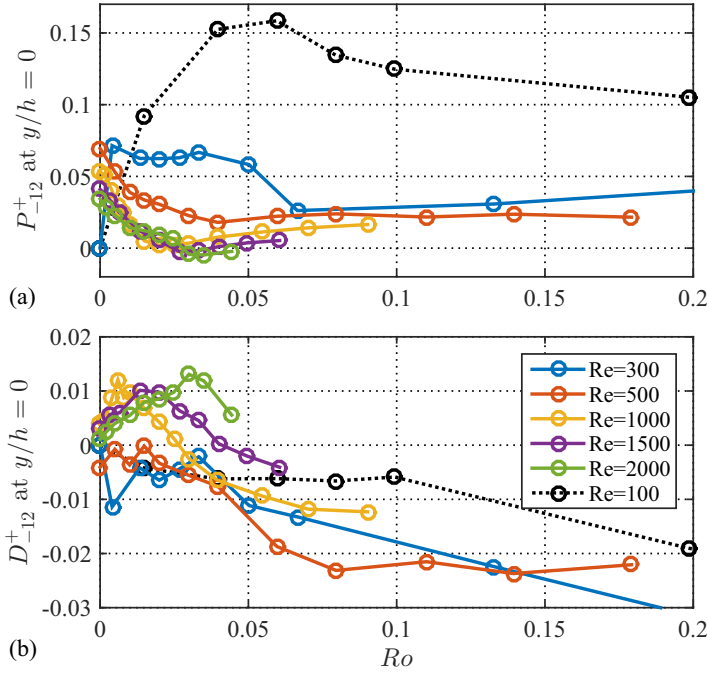


FIG. 21. Variation of the production and turbulent diffusion of the Reynolds shear stress $-\langle uv \rangle^+$ at $y/h = 0$ with the system rotation rate for different Reynolds numbers: (a) the production and (b) the turbulent diffusion.

It is shown in Fig. 20(a) that the profiles of the production terms have a minimum at the channel center and as the Reynolds number increases the production of $-\langle uv \rangle^+$ decreases. Particularly in the cases of $Re = 1000$ – 2000 the $-\langle uv \rangle^+$ production is almost zero at the channel center. Therefore, it is not the $-\langle uv \rangle^+$ production that maintains this anomalous level of the Reynolds shear stress at the channel center.

In Fig. 20(b) it is shown that the magnitude of the turbulent diffusion is not large compared to the production term in general. However, in the case of the high Reynolds numbers $Re = 1000$ – 2000 , the D^+_{-12} profiles have a positive peak at the channel center, which is larger than the production term there. The D^+_{-12} profiles at these Reynolds numbers indicate that the Reynolds shear stress $-\langle uv \rangle^+$ is transported from the near wall region (where D^+_{-12} is negative) to the central region of the channel. The fact that the Reynolds shear stress level slightly exceeds the wall shear stress there is probably due to this transport effect. Indeed, in the lower-Reynolds-number cases, i.e., $Re = 100$, 300 , and 500 , where the negative mean velocity gradient is not observed, the behavior of the turbulent transport term is working in the opposite way: It transports $-\langle uv \rangle^+$ from the central part to the near wall part of the channel.

In Fig. 21 the variations of the production and the turbulent diffusion of $-\langle uv \rangle^+$ on the centerline with the system rotation rate are shown for all the investigated Reynolds-number cases. As shown, in the rotation number range $0.02 \leq Ro \leq 0.04$ the $-\langle uv \rangle^+$ productions in the cases of high Reynolds numbers $Re \geq 1000$ are almost zero, despite the fact that in these Re cases the wall shear stress peak and the negative dU/dy are observed in this Ro range. On the other hand, the D^+_{-12} profiles of the high-Reynolds-number cases $Re \geq 1000$ show positive values at this rotation range, while they turn negative at higher rotation numbers; in particular in the case of $Re = 1500$ and 2000 , D^+_{-12} is positive for the whole intermediate Ro range $0.02 \leq Ro \leq 0.04$, where both the narrow τ_w peak and the negative velocity gradient are observed. On the other hand, those in the lower-Reynolds-number

cases always keep negative values and do not show a positive net transport of $-\langle uv \rangle^+$ at the channel center.

From these results it is reasonable to assume that the transport of $-\langle uv \rangle^+$ towards the central part of the channel by the turbulent transport term results in the anomalous negative velocity gradient at the channel center and the narrow peak of the wall shear stress. This seems to be a unique feature of the high-Reynolds-number cases and only found in a certain low rotation number range.

V. CONCLUSION

In this study the Reynolds and rotation number dependency of the flow structure and the momentum transport of turbulent RPCF are explored. All results indicate that this flow is determined by the rotation in terms of Ro rather than Ω .

The distribution of the turbulent stresses (rms values) in the channel changes with the rotation number. In the center of the channel the value of u_{rms} decreases with increasing Ro , whereas v_{rms} increases. This is in accord with the production term for the Reynolds stresses: The production is negative for $\langle u^2 \rangle$ and positive for $\langle v^2 \rangle$.

The wall shear stress is shown to increase with increasing Reynolds number, as expected, but also with increasing rotation number for low Ro . If the wall shear stress is normalized with the respective turbulent value at zero rotation, all cases collapse on the same curve. This indicates that the increased momentum transfer with rotation increases the shear stress with the same relative amount independent of Re . However, one interesting observation was that the increase with Ro was nonmonotonic for the higher Re studied, which indicates a structural change in the flow around $Ro = 0.02$. A similar observation was made in the numerical study by Salewski and Eckhardt [13], who found a narrow peak of the wall shear stress variation and a negative mean velocity gradient in the center of the channel. We found from an analysis of the Reynolds stress transport equation that there is a transport towards the center of the channel, which may then result in a negative mean velocity gradient there. The results in Refs. [4,6] showing that zero absolute vorticity is established in laminar flows for high enough Reynolds numbers are shown to also extend to turbulent RPCF.

ACKNOWLEDGMENTS

This work was supported by Carl Tryggers Foundation for Scientific Research and KTH.

-
- [1] N. Tillmark and P. H. Alfredsson, in *Advances in Turbulence VI*, edited by S. Gavrilakis, L. Machiels, and P. A. Monkewitz (Kluwer, Dordrecht, 1996), p. 391.
 - [2] P. H. Alfredsson and N. Tillmark, in *Proceedings of the IUTAM Symposium on Laminar-Turbulent Transition and Finite Amplitude Solutions*, edited by T. Mullin and R. Kerswell, Fluid Mechanics and its Applications Vol. 77 (Springer, Berlin, 2005), pp. 173–193.
 - [3] T. Tsukahara, N. Tillmark, and P. H. Alfredsson, Flow regimes in a plane Couette flow with system rotation, *J. Fluid Mech.* **648**, 5 (2010).
 - [4] T. Kawata and P. H. Alfredsson, Experiments in rotating plane Couette flow—momentum transport by roll-cell structure and zero-absolute-vorticity state, *J. Fluid Mech.* **791**, 191 (2016).
 - [5] A. Suryadi, N. Tillmark, and P. H. Alfredsson, Velocity measurements of streamwise roll cells in rotating plane Couette flow, *Exp. Fluids* **54**, 1617 (2013).
 - [6] A. Suryadi, A. Segalini, and P. H. Alfredsson, Zero absolute vorticity: Insight from experiments in rotating laminar plane Couette flow, *Phys. Rev. E* **89**, 033003 (2014).
 - [7] R. Kristoffersen and H. I. Andersson, Direct simulations of low-Reynolds-number turbulent flow in a rotating channel, *J. Fluid Mech.* **256**, 163 (1993).

- [8] O. Grundestam, S. Wallin, and A. V. Johansson, Direct numerical simulation of rotating turbulent channel flow, *J. Fluid Mech.* **598**, 177 (2008).
- [9] Z. Xia, Y. Shi, and S. Chen, Direct numerical simulation of turbulent channel flow with spanwise rotation, *J. Fluid Mech.* **788**, 42 (2016).
- [10] K. H. Bech and H. I. Andersson, Secondary flow in weakly rotating turbulent plane Couette flow, *J. Fluid Mech.* **317**, 195 (1996).
- [11] K. H. Bech and H. I. Andersson, Turbulent plane Couette flow subject to strong system rotation, *J. Fluid Mech.* **347**, 289 (1997).
- [12] M. Barri and H. I. Andersson, Computer experiments on rapidly rotating plane Couette flow, *Commun. Comput. Phys.* **7**, 683 (2010).
- [13] M. Salewski and B. Eckhardt, Turbulent states in plane Couette flow with rotation, *Phys. Fluids* **27**, 045109 (2015).
- [14] N. Tillmark and P. H. Alfredsson, in *Advances in Turbulence 3*, edited by A. V. Johansson and P. H. Alfredsson (Springer, Berlin, 1991), p. 235.
- [15] N. Tillmark and P. H. Alfredsson, Experiments on transition in plane Couette flow, *J. Fluid Mech.* **235**, 89 (1992).
- [16] S. M. Soloff, R. J. Adrian, and Z.-C. Liu, Distortion compensation for generalized stereoscopic particle image velocimetry, *Meas. Sci. Technol.* **8**, 1441 (1997).
- [17] See Supplemental Material at <http://link.aps.org/supplemental/10.1103/PhysRevFluids.1.034402> for movies.
- [18] K. H. Bech, N. Tillmark, P. H. Alfredsson, and H. I. Andersson, An investigation of turbulent plane Couette flow at low Reynolds numbers, *J. Fluid Mech.* **286**, 291 (1995).
- [19] J. Komminaho, A. Lundbladh, and A. V. Johansson, Very large structures in plane turbulent Couette flow, *J. Fluid Mech.* **320**, 259 (1996).
- [20] T. Tsukahara, H. Kawamura, and K. Shingai, DNS of turbulent Couette flow with emphasis on the large-scale structure in the core region, *J. Turbul.* **7**, N19 (2006).
- [21] V. Avsarkisov, S. Hoyas, M. Oberlack, and J. P. García-Galache, Turbulent plane Couette flow at moderately high Reynolds number, *J. Fluid Mech.* **751**, R1 (2014).
- [22] P. Orlandi, M. Bernardini, and S. Pirozzoli, Poiseuille and Couette flows in the transitional and fully turbulent regime, *J. Fluid Mech.* **770**, 424 (2015).
- [23] M. Nagata, Tertiary solutions and their stability in rotating plane Couette flow, *J. Fluid Mech.* **358**, 357 (1998).